Low-threshold terahertz quantum-cascade lasers based on GaAs/$Al_{0.25}Ga_{0.75}As$ heterostructures

M. Wienold,[a] L. Schrottke, M. Giehler, R. Hey, W. Anders, and H. T. Grahn
Paul-Drude-Institut für Festkörperelektronik, Hausvogteiplatz 5-7, 10117 Berlin, Germany

(Received 31 May 2010; accepted 28 July 2010; published online 18 August 2010)

We investigated the influence of the barrier composition on the performance of GaAs-based terahertz (THz) quantum-cascade lasers (QCLs). Based on a nine-quantum-well active region design for 3–4 THz emission, QCLs with an Al content of $x=0.15$ and $x=0.25$ in the $Al_xGa_{1-x}As$ barriers are compared. We found a significantly reduced threshold current density for QCLs with $x=0.25$ as compared to QCLs with $x=0.15$, which is due to a weaker coupling of the subband states. The maximum output power and operating temperature of such lasers are reduced due to the onset of negative differential resistance. © *2010 American Institute of Physics*. [doi:10.1063/1.3480406]

Terahertz (THz) quantum-cascade lasers (QCLs), demonstrated in 2002,[1] are promising coherent light sources for far-infrared spectroscopy and THz imaging.[2] One particular application is THz heterodyne detection of atmospheric and interstellar gases, for which compact continuous-wave (cw) sources with milliwatt level output power are required as local oscillators.[3–5] For practical applications, such lasers can be operated in compact-size Stirling coolers.[6] Due to the limited cooling capacity of such systems, THz QCLs with low threshold currents and low operating voltages are required.

Usually, THz QCL structures rely on GaAs/(Al,Ga)As heterostructures with an Al content of $x=0.10–0.15$ in the barriers. For mid-infrared (MIR) QCLs based on GaAs/(Al,Ga)As, increasing the Al content from $x=0.33$ to $x=0.45$ led to room temperature operation and a reduced parallel conduction at low temperatures, which are both explained by a reduced scattering of confined electrons into continuum states due to the increase in the conduction band offset by 95 meV.[7] However, the operation of a MIR QCL based on purely binary GaAs/AlAs heterostructure has been reported to be limited to cryogenic temperatures due to the onset of negative differential resistance (NDR).[8]

To examine the role of the barrier composition on the performance of THz QCLs, we investigated structures with an Al content of $x=0.15$ and $x=0.25$ in the barriers. The conduction band offset ΔE_c increases in such QCLs by about 80 meV, when the Al content is increased to $x=0.25$. In particular, leakage currents due to thermally activated scattering of electrons into continuum states may affect the maximum operating temperatures and characteristic temperatures of structures, for which the barrier thicknesses are rescaled in order to compensate for the effect of the different Al contents, i.e., conduction band offsets. One possible candidate for deriving such a scaling relation for the barrier heights and thicknesses is the expression for the width of the lowest miniband Δ in a superlattice in the tight-binding limit given by[9]

$$\Delta \propto \exp\left(-L_B\sqrt{\frac{2m^*}{\hbar^2}\Delta E_c}\right), \tag{1}$$

where L_B denotes the barrier width, ΔE_c is the conduction band offset, m^* is the electron effective mass, and $\hbar$ is Planck's constant. From Eq. (1), the following scaling relation is directly obtained:

$$\frac{L_{B,1}}{L_{B,2}} = \sqrt{\frac{\Delta E_{c,2}}{\Delta E_{c,1}}}, \tag{2}$$

where 1 and 2 refer to the Al content of $x=0.15$ and $x=0.25$, respectively.

An analytic expression to estimate the change in the current density, J, for different miniband widths has been derived in Ref. 10. If only the lowest miniband is populated, the expression for scattering-induced miniband transport becomes proportional to $\Delta I_1[\Delta/(k_BT)]/(I_0[\Delta/(k_BT)])$, k_B denotes Boltzmann's constant and T the temperature. I_l refer to the modified Bessel functions. For low temperatures ($k_BT \ll \Delta$), the scaling relationship of the current densities and miniband widths becomes linear $j_1/j_2=\Delta_1/\Delta_2$. This scaling relation can also be obtained from the pioneering work by Esaki and Tsu.[11] In the high temperature limit ($k_BT \gg \Delta$), the above equation results in a quadratic scaling law $j_1/j_2=(\Delta_1/\Delta_2)^2$. This approach gives only a rough estimate of the current scaling behavior, since the injection mechanism in QCLs is not only controlled by intraminiband transport but also by resonant tunneling. In order to use these analytic expressions for QCLs, we assume a superlattice with 12 nm thick wells and 2.5 nm thick barriers (corresponding to an average of the respected layer thicknesses in a typical THz QCL structure). For $x=0.15$, we obtain $\Delta=11$ meV, while for $x=0.25$ it is 7 meV. The calculated current density ratios for the low and high temperature limits are 1.6 and 2.5, respectively. For a temperature of 100 K, the equation results in a value of 2.4.

For our investigations, we chose a design, which has proven to yield high output powers at low biases. The active region consists of nine GaAs quantum wells, forming a cascade of alternating photon and longitudinal optical (LO) phonon-assisted transitions between two quasiminibands.[12] The reference sample R and sample A exhibit the same layer thicknesses but the Al content is $x=0.15$ in sample R and $x=0.25$ in sample A. Sample B contains also $Al_{0.25}Ga_{0.75}As$ barriers but the barrier thicknesses were rescaled according

[a]Electronic mail: wienold@pdi-berlin.de.

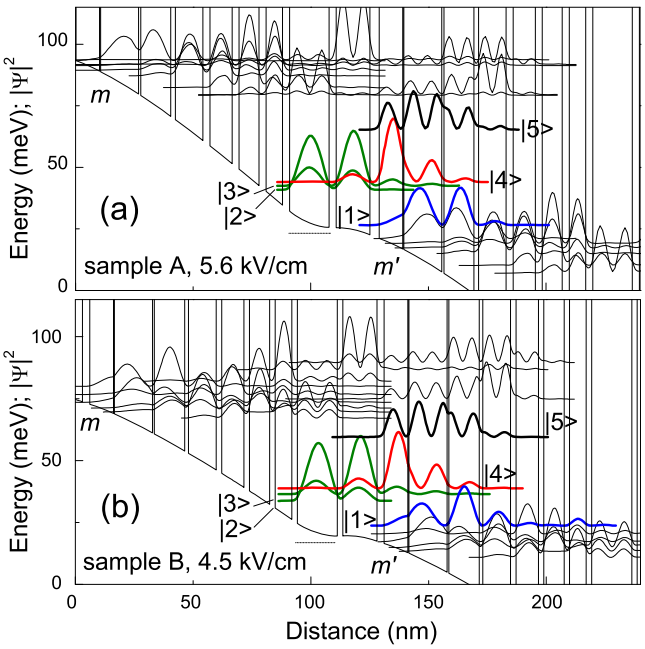

FIG. 1. (Color online) Self-consistent solution of the Schrödinger and Poisson equations (a) for sample A for an applied bias of 5.6 kV/cm and (b) for sample B for an applied bias of 4.5 kV/cm. The layer sequence in nm starting from the injection barrier for sample A and sample R is given by **4**/10.1/**0.5**/16.2/**1**/12.9/**2**/11.8/**3**/9.5/**3**/8.6/**3**/7.1/**3**/17/**3**/14.5. Bold numbers refer to barriers, and the underlined number denotes the Si-doped GaAs layer. The corresponding sequence for sample B is given by **3.08**/10.1/**0.39**/16.2/**0.77**/12.9/**1.54**/11.8/**2.31**/9.5/**2.31**/8.6/**2.31**/7.1/**2.31**/17/**2.31**/14.5.

to Eq. (2) to achieve a similar coupling between subband states as in sample R.

Figures 1(a) and 1(b) depict the results of a band structure calculation for samples A and B, respectively, at their respective threshold, while the result for sample R is shown in Ref. 12. The electrons are transferred from the miniband m into the three subbands labeled $|2\rangle$, $|3\rangle$, and $|4\rangle$ via LO-phonon-assisted scattering. The laser transition takes place between one of the states $|3\rangle$ and $|4\rangle$ and the lower laser level $|1\rangle$, which is part of the extraction/injection miniband m'. Parasitic transport channels arise from nonradiative scattering of electrons from the states $|2\rangle$, $|3\rangle$, and $|4\rangle$ to m' as well as from m to m' via the gap state $|5\rangle$ and from contributions due to the coupling of states of m extending across the injection barrier with excited miniband states of the next period. The results of the band structure calculations are qualitatively very similar for all three samples. However, for samples R and B, the coupling of the subband states is stronger as compared to sample A. The larger coupling results in a larger energy splitting of the states $|2\rangle$, $|3\rangle$, and $|4\rangle$ and also in a larger width of the injection/extraction miniband for the same field strength.

The samples were grown by molecular-beam epitaxy on semi-insulating GaAs substrates. All structures consist of a 300 nm thick GaAs buffer layer, a 700 nm thick highly Si-doped GaAs layer (2×10^{18} cm^{-3}) followed by 85 periods of the active region and an 80 nm thick highly Si-doped GaAs contact layer (5×10^{18} cm^{-3}). The actual values of the layer thicknesses have been confirmed by x-ray diffraction and are within an uncertainty of 3% equal to the nominal values for all lasers. The doping levels in the active region were determined by capacitance-voltage measurements to be about 9×10^{10} cm^{-2} for all samples. After growth, the samples

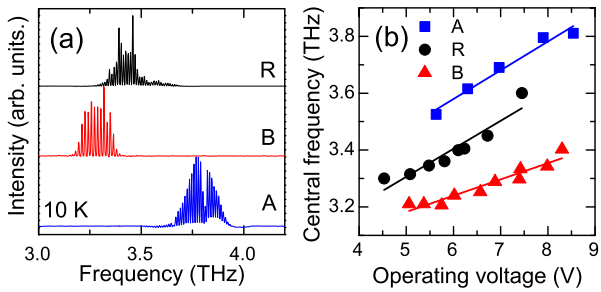

FIG. 2. (Color online) (a) Emission spectra under pulsed operation at 10 K and maximum output power for samples R, B, and A. (b) Central frequency vs voltage of samples A, R, and B for the whole operating temperature regime (5 K$<T<$110 K).

were processed into 100–200 μm wide single plasmon waveguides. As Ohmic contacts, we used AuGe/Ni with a thickness of 200 to 300 nm annealed at 450 °C. Subsequently, lasers were cleaved and attached to copper submounts. For comparison, lasers with similar ridge dimension of about 0.2×3.5 mm^2 for pulsed operation were chosen.

The lasing spectra of samples R, B, and A for a current density at their respective maximum output power (J_{max}) are shown in Fig. 2(a) under pulsed operation (5 kHz, 500 ns). While samples R and B emit around 3.3 to 3.4 THz, the emission of sample A occurs around 3.8 THz. Due to the spatially indirect lasing transition, we observe a Stark shift of the lasing frequency with increasing voltage, independent of operating temperature. The dependence of the central lasing frequency ν_c on operating voltage is shown for all three samples in Fig. 2(b) for the whole operating temperature regime (between 5 and 110 K), which results in an overlap of the emission ranges for the different samples. ν_c can be tuned for each laser over 200 to 300 GHz with the largest tuning range obtained for sample A. The differences in the frequency ranges of the three samples are explained by small differences in the subband alignment due to different barrier heights and widths.

In Fig. 3(a), the threshold current density J_{th} for pulsed

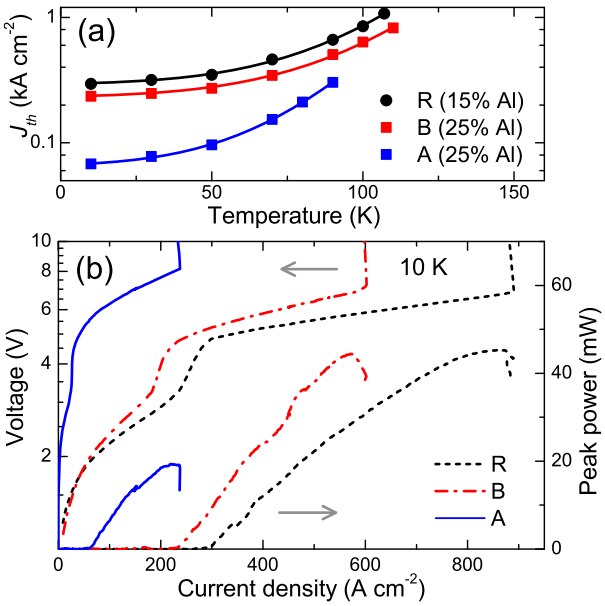

FIG. 3. (Color online) (a) Threshold current density J_{th} vs temperature T for samples R, B, and A under pulsed operation (0.2×3.5 mm^2 laser ridges). (b) LIV characteristics for samples A, B, and R under pulsed operation (0.2×3.5 mm^2 laser ridges).

operation is depicted as function of temperature for samples R, B, and A. At 10 K, J_{th} for sample A is as low as 68 A cm^{-2} as compared to 295 A cm^{-2} for the reference sample R and 235 A cm^{-2} for sample B. The large difference of threshold current densities at low temperature is in contrast to very similar characteristic temperatures T_0. Performing the usual fit to the expression $J_{th}(T)=J_0+J_1\exp(T/T_0)$, values for T_0 of 23.6, 26.1, and 20.4 K are extracted for samples R, B, and A, respectively. Since both the T_0 value and the maximum operating temperature (about 110 K) for sample R and the rescaled sample B are very similar, we conclude that thermally assisted scattering of electrons into continuum states does not result in significant leakage currents in these lasers.

The strongly reduced threshold current of sample A can be qualitatively understood by the reduced coupling of subbands in this structure and hence the reduced parasitic current flow across higher subbands. The differences in the threshold current densities at low temperatures are qualitatively reproduced by numerical simulations incorporating a one-dimensional transport model.[13] The model allows to calculate the current-field characteristics as well as the frequency- and field-dependent material gain. Using the condition for lasing (gain equals losses), the current density at threshold is determined. For the 0.2×3.5 mm^2 cavities, we assumed for the waveguide and mirror losses $\alpha=10$ cm^{-1} and a confinement factor of $\Gamma=0.33$. In addition, the inhomogeneous level broadening was set to 0.5 meV. The calculated threshold current densities for samples R, B, and A are about 200 A cm^{-2}, 120 A cm^{-2}, and 80 A cm^{-2}, respectively, suggesting a reduction in J_{th} for sample A by about a factor of 2.5 as compared to sample R, which is in agreement with the value obtained above in the high-temperature limit. The experimental reduction of J_{th} between samples A and R by a factor of 4 may indicate the existence of additional leakage paths such as tunneling into continuum states, which are not yet included in the model. In contrast to the remarkably reduced threshold current density for sample A at low temperatures, its maximum pulsed operating temperature is reduced to 90 K as compared to 110 K for samples R and B.

Figure 3(b) depicts the pulsed light-current-voltage (LIV) characteristics at 5 K for samples A, B, and R. While samples B and R have comparable levels of peak output power P_{peak} with values of about 45 mW, the peak output power of sample A with a value of 19 mW is significantly smaller, which can be ascribed to the onset of NDR at rather low current densities in this sample. However, the maximum slope efficiency dP_{peak}/dI in the linear regime above threshold is largest for sample A (24.5 mW/A) followed by sample B (21 mW/A) and sample R (16 mW/A). This observation is consistent with the presence of larger parasitic currents in samples R and B as compared to sample A, which in turn reduces the internal quantum efficiency in samples R and B. Larger values for the slope efficiencies have been reported in the literature using a short-period design but at the expense of a much higher operating voltages.[14]

Despite the limitations of sample A under pulsed operation, cw lasers can be obtained with output powers of a few milliwatts. For cw operation, we used a laser from sample A (0.1×1 mm^2 laser ridge). The device operated up to 47 K with a maximum output power of 2.5 mW (1 mW) and $J_{th}=132$ A cm^{-2} (183 A cm^{-2}) at 10 K (40 K), which is still sufficient for applications such as heterodyne spectroscopy. The electrical driving power at threshold is just 0.8 W at 10 K, which is well below the threshold driving power obtained for similar lasers with $Al_{0.15}Ga_{0.85}As$ barriers.[12] Since narrower laser stripes exhibit higher waveguide losses (experimental values: 18 cm^{-1} for 0.1 mm wide and 9 cm^{-1} for 0.2 mm wide lasers) and shorter laser stripes exhibit higher mirror losses, the increase in J_{th} in the cw laser with respect to the pulsed laser is due to both. From a comparison of the $J_{th}(T)$ characteristics for pulsed and cw operation, we find that the effective active region temperature during cw operation is always less than 20 K above its value during pulsed operation. Since there has been no thermal optimization such as substrate thinning, the thermal resistance of 9.3 K/W as determined for this laser might be further reduced.

In conclusion, the threshold current density for a given THz QCL structure can be reduced by as much as a factor of 4 by increasing the Al content from $x=0.15$ to $x=0.25$ in the barriers. This reduction can be explained by a reduced coupling between the subbands in the QCL structure, leading to reduced parasitic currents. From a comparison of these two QCLs with a QCL with $x=0.25$ and rescaled barrier thicknesses, we find no evidence for thermionic leakage currents. However, leakage currents due to tunneling into continuum states might still play a role, which may account for the difference between the experimental and numerical results. We suggest that at least for THz QCLs based on a bound-to-continuum scheme the Al content in the barriers should be considered in addition to the doping density as a parameter for their performance optimization.

[1] R. Köhler, A. Tredicucci, F. Beltram, H. E. Beere, E. H. Linfield, A. G. Davies, D. A. Ritchie, R. C. Iotti, and F. Rossi, Nature (London) **417**, 156 (2002).
[2] B. S. Williams, Nat. Photonics **1**, 517 (2007).
[3] H.-W. Hübers, S. G. Pavlov, A. D. Semenov, R. Köhler, L. Mahler, A. Tredicucci, H. E. Beere, D. A. Ritchie, and E. H. Linfield, Opt. Express **13**, 5890 (2005).
[4] H. Richter, A. D. Semenov, S. G. Pavlov, L. Mahler, A. Tredicucci, H. E. Beere, D. A. Ritchie, K. S. Il'in, M. Siegel, and H.-W. Hübers, Appl. Phys. Lett. **93**, 141108 (2008).
[5] P. Khosropanah, W. Zhang, J. N. Hovenier, J. R. Gao, T. M. Klapwijk, M. I. Amanti, G. Scalari, and J. Faist, J. Appl. Phys. **104**, 113106 (2008).
[6] H. Richter, M. Greiner-Bär, S. G. Pavlov, A. D. Semenov, M. Wienold, L. Schrottke, M. Giehler, R. Hey, H. T. Grahn, and H.-W. Hübers, Opt. Express **18**, 10177 (2010).
[7] H. Page, C. Becker, A. Robertson, G. Glastre, V. Ortiz, and C. Sirtori, Appl. Phys. Lett. **78**, 3529 (2001).
[8] C. Becker, C. Sirtori, H. Page, G. Glastre, V. Ortiz, X. Marcadet, M. Stellmacher, and J. Nagle, Appl. Phys. Lett. **77**, 463 (2000).
[9] G. Bastard, *Wave Mechanics Applied to Semiconductor Heterostructures* (Les Editions de Physique, Les Ulis Cedex, France, 1988).
[10] P. Kleinert and V. V. Bryksin, Physica B **304**, 60 (2001).
[11] L. Esaki and R. Tsu, IBM J. Res. Dev. **14**, 61 (1970).
[12] M. Wienold, L. Schrottke, M. Giehler, R. Hey, W. Anders, and H. T. Grahn, Electron. Lett. **45**, 1030 (2009).
[13] L. Schrottke, M. Giehler, M. Wienold, R. Hey, and H. T. Grahn, Semicond. Sci. Technol. **25**, 045025 (2010).
[14] G. Scalari, M. I. Amanti, M. Fischer, R. Terazzi, C. Walther, M. Beck, and J. Faist, Appl. Phys. Lett. **94**, 041114 (2009).